



Cite this: *J. Mater. Chem. C*, 2018, **6**, 13218

Direct observation of adsorption kinetics on clays by cation– π interaction-triggered aggregation luminescence†

Jinpan Zhong,‡ Xingyu Cui,‡ Weijiang Guan  and Chao Lu *

Luminescence quenching of organic molecules in an aggregation state has become a long-standing challenge for further imaging applications. Inspired by recent research on cation– π interaction triggered luminescence, we designed and synthesized an organic cation, *E*-4-formyl-styryl-pyridinium salt (FSPH), with strong fluorescent emission in the aggregation state. The formation of the FSPH dimer replaces weaker π – π interactions with stronger cation– π interactions to trigger the aggregation luminescence. The excellent optical performances of FSPH in the aggregation state show promise in elucidating the adsorption kinetics of clays because the aggregation of adsorbates during clay adsorption is inevitable. Expectedly, the complete adsorption kinetics of FSPH on clays was visualized by virtue of an *in situ* fluorescence imaging technique. The subsequent fluorescence intensity quantification revealed that the adsorption kinetics of FSPH on clays could be divided into three stages: molecular aggregation at the edge, formation of a block layer, and molecular invasion from the edge to the center. The discovery of the formation of a block layer not only identifies a previously unknown source of the lower adsorption capacity with larger particle sizes of clays, but also inspires the great passion of scientists to study the adsorption kinetics of other adsorbents by employing cation– π interaction-triggered aggregation luminescence.

Received 25th September 2018,
Accepted 6th November 2018

DOI: 10.1039/c8tc04837a

rsc.li/materials-c

Introduction

It has been widely reported that the strong electrostatic attraction between the negatively-charged π -electron cloud and a positively-charged cation could generate cation– π interaction.^{1,2} Over the past few decades, cation– π interaction has played a dominant role in many forefront areas of modern chemistry, from materials design to molecular biology.^{3–6} Recent research studies reported that the intermolecular cation– π interaction between an amine cation and tryptophan could trigger visible absorbance and fluorescence.^{7,8} This discovery is considered to have great potential in the imaging field. However, the reported systems usually require the cation– π interaction to be between two types of molecules, limiting their practical application. In addition, the low quantum yield of solid-state fluorescence of these systems is difficult to detect using the existing imaging techniques. Therefore, the design and synthesis of novel molecules with strong solid-state luminescence triggered by cation– π

interactions are regarded as the most promising solution. Herein, we synthesized *E*-4-formyl-styryl-pyridine (FSP) through a one-step reaction.^{9,10} Once FSP gets protonated into the *E*-4-formyl-styryl-pyridinium salt (FSPH) *via* simple acidification, highly-efficient blue emissions were observed in the aggregation state as a result of the replacement of weaker π – π interactions by stronger cation– π interactions. Such strong solid-state fluorescence makes FSPH an ideal cationic dye for imaging applications.

A clear understanding of adsorption kinetics has become a long-term challenge because direct visualization of adsorption processes is hard to achieve. The major obstacle for the visualization of adsorption by luminescence is the inevitable quenching of traditional dyes in the aggregation state.^{11–13} Therefore, the design of a specific adsorption process involving the strong fluorescence of FSPH in the aggregation state is considered to be a rational solution. For adsorption of cationic dyes, the most suitable host material is a negatively charged clay, due to its chemical stability, high surface area and large cation exchange capacity.^{14–17} Typically, electron microscopy and X-ray diffraction patterns are suitable for describing the final state of an adsorption process.^{18,19} In addition, molecular dynamics simulation is applied to interpret the interlayer interaction at the molecular level and the thermodynamic process of

State Key Laboratory of Chemical Resource Engineering, Beijing University of Chemical Technology, Beijing 100029, China. E-mail: luchao@mail.buct.edu.cn

† Electronic supplementary information (ESI) available. CCDC 1812126. For ESI and crystallographic data in CIF or other electronic format, see DOI: 10.1039/c8tc04837a

‡ These authors contributed equally.

the simulated system.^{20–23} Although these methods could provide some information about the adsorption process of the clay, the precise adsorption mechanism is poorly understood due to the lack of direct observation of adsorption kinetics. Therefore, it is highly significant to establish an *in situ* visualization method for adsorption processes of clays. It is anticipated that FSPH could act as an ideal cationic dye for investigating adsorption kinetics on clays through real-time recording.

Confocal laser scanning microscopy (CLSM) allows the ultrafast and real-time observation of the chemical reaction process and dynamic structural transition, benefiting from its non-invasive, macroscale and high-contrast scanning.^{24–28} This simple and powerful technique of CLSM inspired us to observe the *in situ* adsorption process of FSPH on clays. The invasion of FSPH dye from the edge to the center of the clay was directly observed during the adsorption process. The subsequent time-varying fluorescence intensity quantification demonstrated that the adsorption process of FSPH could be divided into three stages: molecular aggregation at the edge, formation of a block layer, and molecular invasion from the edge to the center. More importantly, we found that a larger particle size of the clay could lead to a lower adsorption efficiency. Our established method presents direct evidence for the adsorption mechanism.

Results and discussion

The most common interaction of organic dyes in the aggregation state is the π - π interaction between conjugated segments. This π - π interaction usually results in the aggregation-caused quenching (ACQ) of fluorescence.^{29–31} As depicted in Fig. S1 (ESI[†]), FSP was easily synthesized *via* a one-step Heck coupling reaction between 4-vinylpyridine and 4-bromobenzaldehyde. The pyridine group in FSP was easily cationized by adding an excess of acid to form FSPH. The molecular structures of FSP and FSPH were verified by ¹H nuclear magnetic resonance (NMR) spectroscopy (Fig. S2 and S3, ESI[†]) and mass spectroscopy (Fig. S4, ESI[†]).

There is only one cation difference in the molecular structures of FSP and FSPH, but their fluorescence behaviours in the aggregation state were completely different. As shown in the inset of Fig. 1, upon photoexcitation by ultraviolet light at 365 nm, the drop-cast film of FSPH could generate intense fluorescence, while the FSP film showed faint fluorescence. In addition, Fig. 1 indicates that two weak emission peaks at 430 and 460 nm were detected in FSP. On the other hand, FSPH displayed a 6-fold increase in luminescence intensity with a single peak at 485 nm. Moreover, to remove the effect of the film thickness on the fluorescence intensity, the fluorescence quantum yields of FSP and FSPH films were also determined using a steady-state fluorescence spectrometer with an integrating sphere. It was found that the quantum yields of FSPH and FSP were 19.60% and 2.23%, respectively, which was consistent with their fluorescence intensities. Therefore, it can be concluded that the introduction of cations could lead

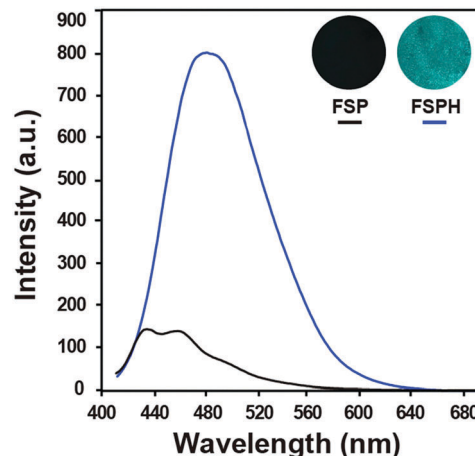


Fig. 1 Fluorescence spectra of FSP (black line) and FSPH (blue line) films. Inset: Fluorescence photographs of FSP and FSPH films under a UV lamp at 365 nm.

to a significant improvement in the aggregation-state luminescence efficiency.

The electronic transitions from the molecular ground states to the excited states of FSP and FSPH were studied in detail using their UV-visible absorption spectra in dilute tetrahydrofuran solutions and solid films, respectively.³² As shown in Fig. 2a, the solutions of FSP and FSPH displayed an absorption peak at 324 nm. Unlike the case of the absorption spectra in solutions, the maximum absorption wavelength of the FSPH film was obviously red-shifted in comparison with that of the FSP film (Fig. 2b). In order to explain this difference, the electronic energy states were further investigated by calculating the highest occupied molecular orbital (HOMO) and the lowest unoccupied molecular orbital (LUMO) of SPH and FSPH in the ground state.^{33–35} As depicted in Fig. 2c, the HOMO and LUMO of FSPH monomer were partially localized on the benzaldehyde group and the pyridinium group.^{36–38} The formation of FSPH dimers in solid films could reduce the energy gaps of the FSPH monomers in solutions from 2.20 eV to 2.05 eV. The decreased energy gaps would induce the red-shift of absorption in the solid films. These results were in good agreement with those obtained by the measured absorption wavelengths. In conclusion, the electronic energy state of the FSPH solid film is greatly different from that of its solution, resulting from the much stronger interactions in the aggregation state.

The intermolecular stacking in the solid state was investigated by the characterization of single crystals of FSP and FSPH, respectively. A single crystal of FSP was obtained from previous references, and the FSPH single crystal was cultivated by slow evaporation of its ethanol solution (Tables S1–S7, ESI[†]).^{9,39} Fig. 3a shows that FSP molecules were packed in a face-to-face parallel alignment with a large θ angle of 76°, leading to a strong π - π interaction. In contrast, FSPH molecules could form a head-to-tail packing structure through the strong cation- π interaction between pyridinium cations and phenyl rings (Fig. 3b). The distance between pyridinium cation and aromatic ring in the FSPH single crystal was $d = 3.5299$ Å.

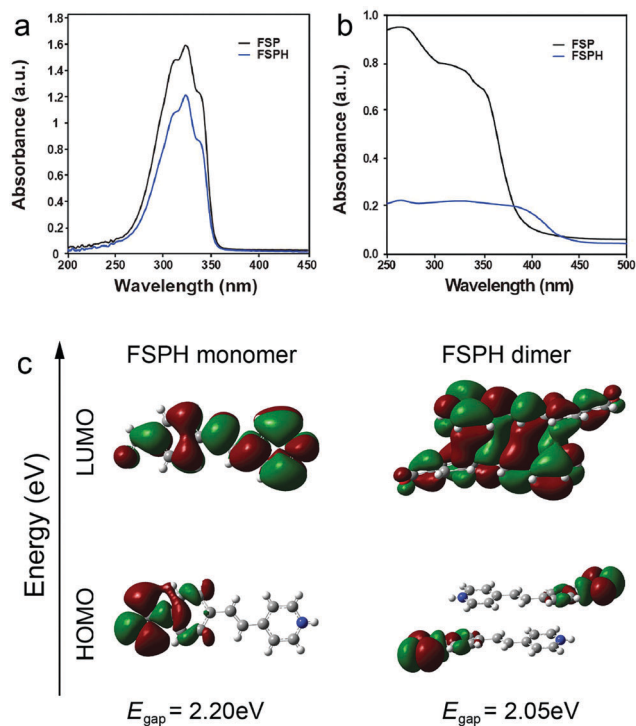


Fig. 2 (a) Absorption spectra of 50 μM FSP and 50 μM FSPH in tetrahydrofuran solution. (b) Absorption spectra of films of FSP and FSPH. (c) Calculated HOMO and LUMO of FSPH monomers and FSPH dimers in the ground state. Calculated using TD-DFT, B3LYP/6-31G**, and the Gaussian 09 program.

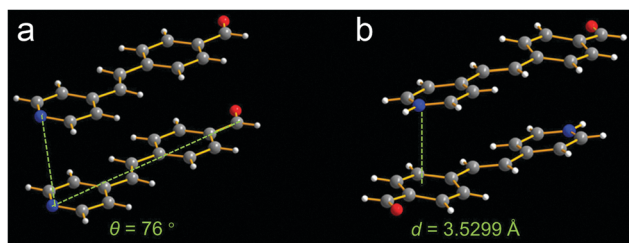


Fig. 3 Intermolecular stacks of (a) FSP and (b) FSPH. Blue, red, grey, and white balls represent N, O, C, and H atoms, respectively.

In combination with the efficiency of its solid-state luminescence, it was concluded that stronger cation- π interactions could replace weaker π - π interactions in the solid state, achieving a better aggregation-state luminescence efficiency. In conclusion, the combination of fluorescence, UV-visible absorption, single crystal and electronic energy state data indicated that the organic aggregation-state luminescence efficiency could be modulated by tuning intermolecular cation- π stacking interactions.

The cation- π interaction-induced fluorescence enhancement in the aggregation state makes FSPH an ideal indicator for *in situ* visualization of adsorption kinetics of clays. Montmorillonite (MMT), a clay with layers composed of one alumina sheet sandwiched by two silica sheets, was applied for the adsorption of FSPH.¹⁴ 100 μL of a supernatant stock solution (10 mg of MMT dissolved in 5 mL of methanol) was dropped into a confocal dish.

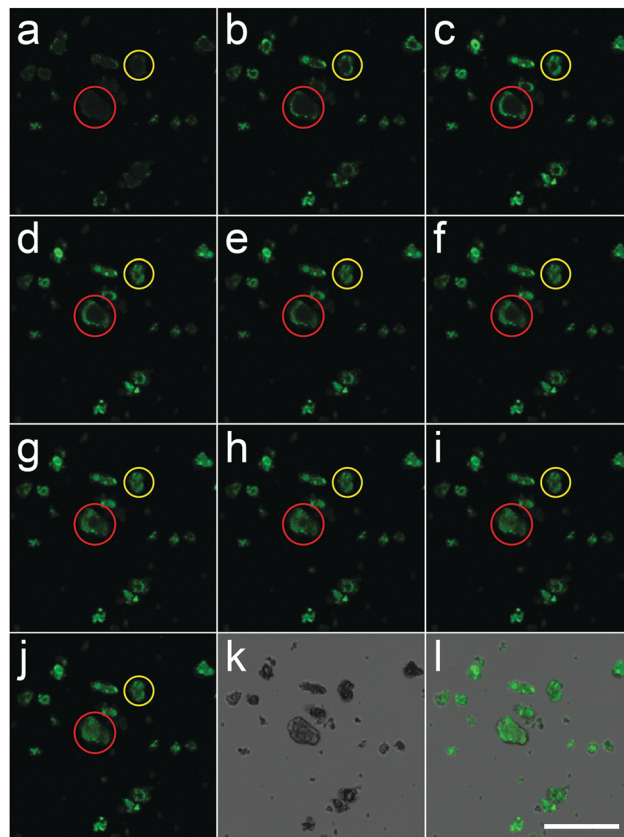


Fig. 4 A 12-minute video of 200 μM FSPH adsorbed by MMT was recorded. (a–j) Time interval between two images is 77.25 seconds. (k and l) Brightfield and overlay images of (j), scale bar: 50 μm , object lens: 20, excitation laser diode: 405 nm. Red circle: large MMT platelets, yellow circle: small MMT platelets.

Upon evaporation of methanol at 60 $^\circ\text{C}$, the individual MMT platelets were distributed in the dish without aggregation. The cation exchange capacity of MMT was 80 mequiv per 100 g and thus the exchangeable molar quantity of cations was around 0.16 μmol . For observation of the complete adsorption of MMT, the excess loading of 1.0 mL of FSPH solution (200 μM) was added into the confocal dish. The injection of FSPH solution was performed using a micro-syringe along the lateral wall in order to keep the MMT platelets immobile as much as possible. Once the MMT platelets were wetted by the FSPH solution, the video recording was started using CLSM.

As shown in Fig. 4a, the green fluorescence of FSPH was immediately generated once the FSPH solution reached the edge of MMT. Negatively charged MMT layers could adsorb the FSPH cations from the solution by electrostatic interaction, resulting in the rapid aggregation of FSPH. Therefore, the turn-on green fluorescence was observed along the edge of MMT because of the cation- π interaction-triggered molecular stacking. From Fig. 4a–j, the invasion of green fluorescence from the edge to the center of MMT was observed with increasing loading time. Such a phenomenon illustrated the *in situ* adsorption process of FSPH cations into MMT from the edge to the center. However, the adsorption rate obviously varied for MMT

with different particle sizes. For example, the adsorption time of the MMT platelet in the red circle (12 minutes) is nearly twice that in the yellow circle (6 minutes). Swelling in water is an inherent property of montmorillonite, leading to the expansion of interlayer spacing. For larger MMT platelets, the swelling process is more difficult because the penetration of water molecules is limited. Therefore, adsorption of FSPH dissolved in water preferentially occurred at the edge of MMT. In addition, the distance between the edge and the center is longer for larger MMT platelets, and thus FSPH takes a longer time to reach the center.

To investigate the intrinsic adsorption kinetics of MMT, time-resolved fluorescence analysis was obtained by quantification of the video frame-by-frame. As shown in Fig. 5a, a gradual invasion of fluorescence signals from the edge to the center of MMT was observed over time. All the MMT platelets remained immobile during the video recording and therefore the time-varying fluorescence intensity of selected locations could be exported. A straight line was drawn from the edge to the center of MMT and ten locations (L) with equidistance were selected along this line (Fig. 5b). Subsequently, the time-varying fluorescence intensities of the corresponding ten locations in Fig. 5b were exported *via* CLSM (Fig. 5c). Interestingly, if the fluorescence intensity variation of the ten locations was studied as a whole, the total adsorption of FSPH could be divided into three stages (Fig. 5d1–d3). In the first stage of molecular aggregation, the fluorescence intensity of L1, L2 and L3 at the edge of the MMT platelets increased sharply with the increase of time

(Fig. 5d1). Once the FSPH solution reached the edge of MMT, the exchangeable sodium ions diffused into water instantly, leading to the expansion of interlayer spacing. Then, a large number of FSPH molecules adsorbed at the edge of MMT by electrostatic interaction, compensating for the sodium ions. As the degree of swelling decreased from the edge to the center, the increasing rate of fluorescence intensity decreased from L3 to L6. This phenomenon indicated that most of the FSPH molecules aggregated at the outermost edge at the first stage of adsorption. In addition, the observation of molecular aggregation at the edge was consistent with the results from former research.^{18,22,40} In the second stage of the formation of a block layer, the fluorescence intensity of L3 gradually decreased while the fluorescence intensity of L4 reached maximum. Afterwards, the fluorescence intensity of L4 slightly decreased and the fluorescence intensity of L5 reached maximum. Meanwhile, an increase of fluorescence intensity was observed from L6 to L10. This unusual process indicated the existence of a unique molecular movement during the clay adsorption of organic cations. When FSPH cations adsorbed into the interlayer of MMT through electrostatic interactions, a block layer with FSPH cations formed at the same time. This block layer performed as a barrier to prevent the entrance of water because of the strong hydrophobicity of the organic matter. Therefore, further adsorption of the rest of the dissolved FSPH in the solution was inhibited by the block layer. In the third stage of the molecular invasion from the edge to the center, the fluorescence intensity from L2 to L6 decreased while the fluorescence intensity from L7 to L10 increased. The reduced fluorescence intensity of L2 and L3 demonstrated that FSPH molecules were re-dissolved from the edge of MMT into the solution, and thus the adsorption of FSPH from the solution finished. Meanwhile, the aggregated FSPH in the block layer gradually invaded into the center of MMT and finally reached a balance. This stage is in accordance with the previously reported diffusion process of adsorbates during clay adsorption.^{22,41}

The effects of platelet size on the adsorption kinetics were examined (Fig. 6 and Fig. S5, S6, ESI†). As shown in Fig. 6a, the invasion of FSPH from the edge to the center of MMT was no different from the process given in Fig. 5a. However, the image of the final state indicated that the fluorescence intensity of the center was much weaker than that of the edge. Accordingly, the same quantification process was applied to explain this difference. As shown in Fig. 6d1–d3, the three stages of adsorption were also similar to those of the MMT platelets of smaller particle size. The only difference was that the final fluorescence intensity from L14 to L28 was much lower than the fluorescence intensity from L8 to L10. This difference could be explained by the established model of a block layer. The block layer of FSPH in the second stage could prevent further adsorption of FSPH from the solution. Then, in the third stage, FSPH cations could move from the block layer at the edge to the center. For larger MMT platelets, the distance between the edge and the center is much longer and thus the amount of FSPH in the block layer is unable to fill up the interior part of MMT. As a result, a gradual decrease of fluorescence intensity was observed from the edge to the center. In conclusion, MMT platelets with larger sizes

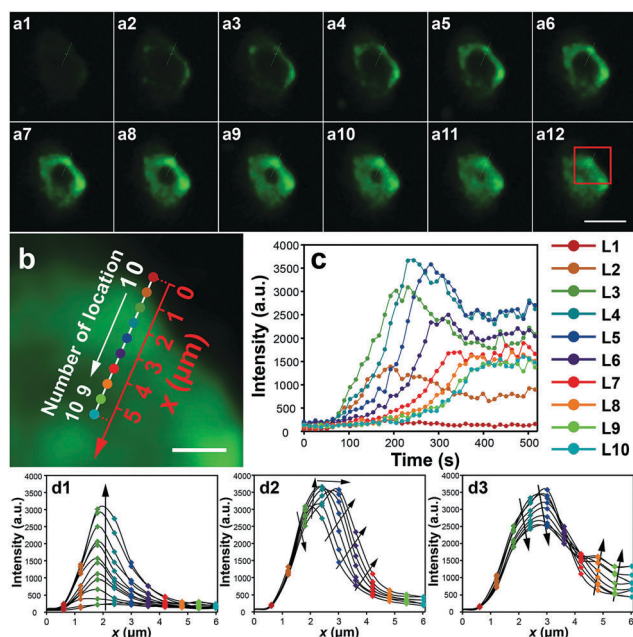


Fig. 5 (a1–a12) Time-varying fluorescence distribution of FSPH within MMT, scale bar: 10 μm . (b) Selected locations along the straight line from the edge to the center for the quantification of fluorescence intensity; enlarged image of the red square in (a12), scale bar: 2 μm . (c) Time-varying fluorescence intensity of the numbered locations in (b), time interval between two dots: 12.875 seconds. (d1–d3) Three stages of time-varying fluorescence intensity of ten locations along the x -axis in (b), time interval between two curves: 12.875 seconds.

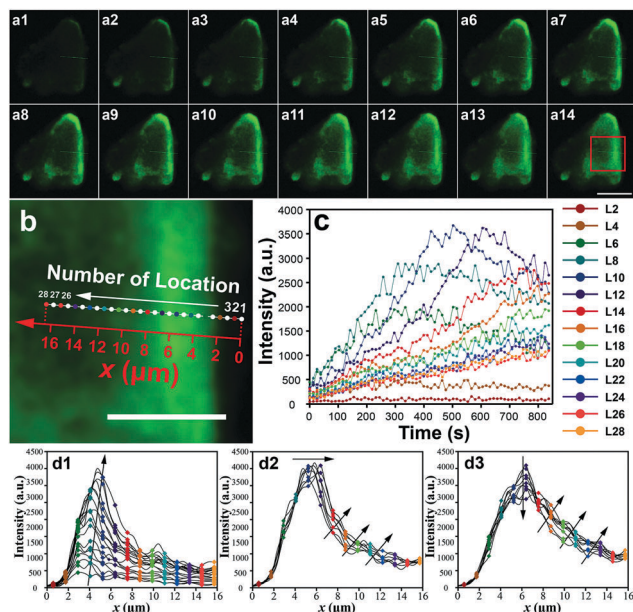


Fig. 6 (a1–a12) Time-varying fluorescence distribution of FSPH within MMT, scale bar: 20 μm . (b) Selected locations along the straight line from the edge to the center for quantification of fluorescence intensity; enlarged image of the red square in (a12), scale bar: 10 μm . (c) Time-varying fluorescence intensity of the numbered locations in (b), time interval between two dots: 12.875 seconds. (d1–d3) Three stages of time-varying fluorescence intensity of fourteen locations along the x-axis in (b), time interval between two curves: 12.875 seconds.

have a lower adsorption efficiency because the interior part could not be completely utilized.

Conclusions

In conclusion, the high luminescence efficiency of the as-prepared FSPH is achieved by replacing weaker π - π interactions with stronger cation- π stacking, leading to the formation of dimers with a higher rigidity in the aggregation state. The *in situ* adsorption kinetics of FSPH on clays was directly visualized by video-recording of CLSM. The detailed adsorption kinetics was interpreted by quantification of the time-varying fluorescence intensity of FSPH in the interlayer of MMT. The concept of a block layer was proposed to explain the unique phenomena in the adsorption mechanism. Subsequent data analysis revealed that clay platelets with smaller particle sizes could lead to higher adsorption efficiency because the block layer hampers the invasion of FSPH to the center of the clay. Therefore, the design and synthesis of novel cationic dyes with strong luminescence triggered by cation- π interactions and the establishment of a corresponding imaging strategy could open new opportunities and provide inspiration for visualization of more sophisticated chemical reaction processes.

Experimental section

Chemicals and materials

4-Bromobenzaldehyde and palladium diacetate ($\text{Pd}(\text{OAc})_2$) were purchased from SA EN Chemical Technology Co., Ltd

(Shanghai, China). 4-Vinylpyridine and anhydrous potassium phosphate were obtained from Alfa Aesar, Thermo Fisher Scientific Inc. (Shanghai, China). Anhydrous dimethyl formamide (DMF) was supplied by J&K Chemical Ltd (Beijing, China). Tetrahydrofuran (THF), 37% hydrochloric acid (HCl), dimethylsulfoxide (DMSO), dichloromethane (DCM), petroleum ether (PE), methanol, ethanol, acetone, trifluoroacetate, and anhydrous sodium sulfate were analytically pure and purchased from Beijing Chemical Reagent Company (Beijing, China). Deionized water was freshly prepared from a Millipore Milli-Q system with 18.2 MU cm^{-1} resistivity (Barnstead, CA, USA). Sodium montmorillonite (Na^+ -MMT) with a cation exchange capacity value of 145 meq per 100 g (from Nanocor, PGW grades) was used without further purification.

Synthesis of *E*-4-formyl-styryl-pyridine (FSP)

4-Bromobenzaldehyde (1.11 g, 6.0 mmol), $\text{Pd}(\text{OAc})_2$ (0.12 g, 0.5 mmol), and anhydrous potassium phosphate (3.82 g, 18.0 mmol) were put into a two-necked flask (100 mL) with a magnetic stir bar and a condenser tube. The flask was evacuated using an oil pump and purged with nitrogen gas three times. Dry anhydrous DMF (40 mL) was then added under a nitrogen atmosphere and the mixture was dissolved completely. When the temperature of the oil bath reached 125°C , 4-vinylpyridine (1.51 g, 14.4 mmol) was injected dropwise and reacted for 12 h. Upon cooling down to room temperature, the reaction solution was extracted three times using DCM (40 mL). The organic layers were collected and washed with deionized water thrice, and further dried by anhydrous sodium sulfate. Finally, the crude product was purified using silica-gel chromatography: the eluent was a mixed solution of PE and acetone (v/v 4:1), and pure FSP was obtained with a yield of 0.48 g. $^1\text{H NMR}$ (400 MHz, DMSO-d_6 , δ): 10.01–10.02 (s, 1H), 8.57–8.61 (d, 2H), 7.93–7.98 (d, 2H), 7.86–7.91 (d, 2H), 7.63–7.69 (d, 1H), 7.59–7.63 (d, 2H), 7.44–7.51 (d, 1H).

Synthesis of *E*-4-formyl-styryl-pyridinium salt (FSPH)

To obtain the protonated products of FSP, pure FSP (0.10 g) was weighed and put into two 3 mL vials separately. Then, an excess amount of HCl (1.0 M, 1 mL) was added to dissolve and react with FSP at room temperature for 4 h. When the residual HCl was removed by vacuum-rotary evaporation, SPH and FSPH could be obtained with a high yield of over 90%. $^1\text{H NMR}$ of FSPH (400 MHz, DMSO-d_6 , δ): 10.05–10.07 (s, 1H), 8.88–8.93 (d, 2H), 8.24–8.31 (d, 2H), 8.07–8.14 (d, 1H), 8.00–8.05 (d, 2H), 7.95–7.99 (d, 2H), 7.00–7.09 (d, 1H). MS of FSPH: m/z : 210.0921 ($[\text{M} - \text{Cl}]^+$, calculated for $\text{C}_{14}\text{H}_{12}\text{NO}$, 210.0919).

Sample characterization

Proton nuclear magnetic resonance ($^1\text{H NMR}$) spectra were recorded by using a 400 MHz Bruker spectrometer (Germany). Mass spectroscopy (MS) was accomplished using a Waters Quattro microtriple quadrupole mass spectrometer (USA). The UV-vis absorption spectra were recorded using a Shimadzu UV-3600 spectrophotometer (Japan). Fluorescence spectra were measured using a Hitachi F-7000 fluorescence spectrophotometer (Japan).

The excitation and emission slits were both set at 5.0 nm with a scanning rate of 1200 nm min⁻¹. X-ray diffraction intensity data were collected on a Rigaku-Oxford Gemini E diffractometer. Fluorescence images and intensity quantification data were obtained using a Leica TCS SP8 confocal laser scanning microscope (Germany). The quantum yields were recorded on an Edinburgh FLS 980 steady state spectrometer equipped with an integrating sphere.

Computational details

Theoretical calculations were carried out using TD-DFT, B3LYP/6-31G**, and the Gaussian 09 program package.^{34,35,42–48} Monomers and dimers used to do the ground-state calculations were obtained from the crystal structures of SPH and FSPH. Excited-state simulation for SP and FSP was performed in the gas phase.

Conflicts of interest

There are no conflicts to declare.

Acknowledgements

This work was supported by the National Basic Research Program of China (the 973 Program, 2014CB932103), the National Natural Science Foundation of China (21656001, 21521005, 21575010 and 21701004), and the Innovation and Promotion Project of Beijing University of Chemical Technology.

Notes and references

- J. C. Ma and D. A. Dougherty, *Chem. Rev.*, 1997, **97**, 1303–1324.
- D. A. Dougherty, *Acc. Chem. Res.*, 2013, **46**, 885–893.
- A. S. Mahadevi and G. N. Sastry, *Chem. Rev.*, 2013, **113**, 2100–2138.
- K. Fujisawa, M. Humbert-Droz, R. Letrun, E. Vauthey, T. A. Wesolowski, N. Sakai and S. Matile, *J. Am. Chem. Soc.*, 2015, **137**, 11047–11056.
- D. Q. Yang, Y. G. Wang, D. X. Liu, Z. Q. Li and H. R. Li, *J. Mater. Chem. C*, 2018, **6**, 1944–1950.
- A. J. Neel, M. J. Hilton, M. S. Sigman and F. D. Toste, *Nature*, 2017, **543**, 637–646.
- W.-L. Zhu, X.-J. Tan, C. M. Pua, J.-D. Gu, H.-L. Jiang, K.-X. Chen, C. E. Felder, I. Silman and J. L. Sussman, *J. Phys. Chem. A*, 2000, **104**, 9573–9580.
- L. J. Juszcak and A. S. Eisenberg, *J. Am. Chem. Soc.*, 2017, **139**, 8302–8311.
- S. Yamada, N. Uematsu and K. Yamashita, *J. Am. Chem. Soc.*, 2007, **129**, 12100–12101.
- T. Sakamoto, Y. Nishimura, T. Nishimura and T. Kato, *Angew. Chem., Int. Ed.*, 2011, **50**, 5856–5859.
- L. D. Lu, R. M. Jones, D. McBranch and D. Whitten, *Langmuir*, 2002, **18**, 7706–7713.
- V. Martínez Martínez, F. López Arbeloa, J. Bañuelos Prieto and I. López Arbeloa, *J. Phys. Chem. B*, 2005, **109**, 7443–7450.
- F. López Arbeloa, V. Martínez Martínez, T. Arbeloa and I. López Arbeloa, *J. Photochem. Photobiol., C*, 2007, **8**, 85–108.
- K. G. Bhattacharyya and S. S. Gupta, *Adv. Colloid Interface Sci.*, 2008, **140**, 114–131.
- N. Miyamoto, R. Kawai, K. Kuroda and M. Ogawa, *Appl. Clay Sci.*, 2000, **16**, 161–170.
- Y. Park, G. A. Ayoko and R. L. Frost, *J. Colloid Interface Sci.*, 2011, **354**, 292–305.
- C.-C. Wang, L.-C. Juang, T.-C. Hsu, C.-K. Lee, J.-F. Lee and F.-C. Huang, *J. Colloid Interface Sci.*, 2004, **273**, 80–86.
- D. Yaron-Marcovich, Y. Chen, S. Nir and R. Prost, *Environ. Sci. Technol.*, 2005, **39**, 1231–1238.
- H. P. He, R. L. Frost, T. Bostrom, P. Yuan, L. Duong, D. Yang, Y. F. Xi and J. T. Klopogge, *Appl. Clay Sci.*, 2006, **31**, 262–271.
- Q. Zhao and S. E. Burns, *Environ. Sci. Technol.*, 2012, **4**, 3999–4007.
- Q. Zhou, R. L. Zhu, S. C. Parker, J. X. Zhu, H. P. He and M. Molinari, *RSC Adv.*, 2015, **5**, 47022–47030.
- T. V. Shapley, M. Molinari, R. L. Zhu and S. C. Parker, *J. Phys. Chem. C*, 2013, **117**, 24975–24984.
- E. J. M. Hensen, T. J. Tambach, A. Blik and B. Smit, *J. Chem. Phys.*, 2001, **115**, 3322–3329.
- J. Huang, H. Wang, X. H. Yang, K. Quan, Y. J. Yang, L. Ying, N. L. Xie, M. Ou and K. M. Wang, *Chem. Sci.*, 2016, **7**, 3829–3835.
- D. L. Fu, J. E. Schmidt, Z. Ristanović, A. D. Chowdhury, F. Meirer and B. M. Weckhuysen, *Angew. Chem., Int. Ed.*, 2017, **56**, 11217–11221.
- K. Han, D. Go, T. Tigges, K. Rahimi, A. J. C. Kuehne and A. Walther, *Angew. Chem., Int. Ed.*, 2017, **56**, 2176–2182.
- Q. M. Liu, Q. Xia, S. Wang, B. S. Li and B. Z. Tang, *J. Mater. Chem. C*, 2018, **6**, 4807–4816.
- A. Ummadisingu, L. Steier, J.-Y. Seo, T. Matsui, A. Abate, W. Tress and M. Grätzel, *Nature*, 2017, **545**, 208–212.
- W. J. Guan, W. J. Zhou, J. Lu and C. Lu, *Chem. Soc. Rev.*, 2015, **44**, 6981–7009.
- H. K. Zhang, X. Y. Zheng, N. Xie, Z. K. He, J. K. Liu, N. L. C. Leung, Y. L. Niu, X. H. Huang, K. S. Wong, R. T. K. Kwok, H. H. Y. Sung, I. D. Williams, A. J. Qin, J. W. Y. Lam and B. Z. Tang, *J. Am. Chem. Soc.*, 2017, **139**, 16264–16272.
- I. Shulov, R. V. Rodik, Y. Arntz, A. Reisch, V. I. Kalchenko and A. S. Klymchenko, *Angew. Chem., Int. Ed.*, 2016, **55**, 15884–15888.
- T. Owen, *Fundamentals of UV-Visible Spectroscopy, A Primer*, Hewlett-Packard Company, Böblingen, Germany, 1996.
- Q. Peng, H. Yan, X. H. Zhang and Y.-D. Wu, *J. Org. Chem.*, 2012, **77**, 7487–7496.
- G. A. Petersson, A. Bennett, T. G. Tensfeldt, M. A. Al-Laham, W. A. Shirley and J. Mantzaris, *J. Chem. Phys.*, 1988, **89**, 2193–2218.
- M. J. Frisch, G. W. Trucks, H. B. Schlegel, G. E. Scuseria, M. A. Robb, J. R. Cheeseman, J. A. Montgomery, Jr., T. Vreven, K. N. Kudin, J. C. Burant, J. M. Millam, S. S. Iyengar, J. Tomasi, V. Barone, B. Mennucci, M. Cossi, G. Scalmani, N. Rega, G. A. Petersson, H. Nakatsuji,

- M. Hada, M. Ehara, K. Toyota, R. Fukuda, J. Hasegawa, M. Ishida, T. Nakajima, Y. Honda, O. Kitao, H. Nakai, M. Klene, X. Li, J. E. Knox, H. P. Hratchian, J. B. Cross, C. Adamo, J. Jaramillo, R. Gomperts, R. E. Stratmann, O. Yazyev, A. J. Austin, R. Cammi, C. Pomelli, J. W. Ochterski, P. Y. Ayala, K. Morokuma, G. A. Voth, P. Salvador, J. J. Dannenberg, V. G. Zakrzewski, S. Dapprich, A. D. Daniels, M. C. Strain, O. Farkas, D. K. Malick, A. D. Rabuck, K. Raghavachari, J. B. Foresman, J. V. Ortiz, Q. Cui, A. G. Baboul, S. Clifford, J. Cioslowski, B. B. Stefanov, G. Liu, A. Liashenko, P. Piskorz, I. Komaromi, R. L. Martin, D. J. Fox, T. Keith, M. A. Al-Laham, C. Y. Peng, A. Nanayakkara, M. Challacombe, P. M. W. Gill, B. Johnson, W. Chen, M. W. Wong, C. Gonzalez and J. A. Pople, *Gaussian 03, Revision C.02 & D.01*, Gaussian, Inc., Wallingford, CT, 2004.
- 36 Z. Q. Liu, J. S. A. Ishibashi, C. Darrigan, A. Dargelos, A. Chrostowska, B. Li, M. Vasiliu, D. A. Dixon and S.-Y. Liu, *J. Am. Chem. Soc.*, 2017, **139**, 6082–6085.
- 37 I. N. Ioffe, M. Quick, M. T. Quick, A. L. Dobryakov, C. Richter, A. A. Granovsky, F. Berndt, R. Mahrwald, N. P. Ernstring and S. A. Kovalenko, *J. Am. Chem. Soc.*, 2017, **139**, 15265–15274.
- 38 D. D. Burns, K. L. Teppang, R. W. Lee, M. E. Lokensgard and B. W. Purse, *J. Am. Chem. Soc.*, 2017, **139**, 1372–1375.
- 39 G. Soriano-Moro, M. J. Percino, A. L. Sanchez, V. M. Chapela, M. Ceron and M. E. Castro, *Molecules*, 2015, **20**, 5793–5811.
- 40 E. M. Pecini and M. J. Avena, *Langmuir*, 2013, **29**, 14926–14934.
- 41 A. Kausar, M. Iqbal, A. Javed, K. Aftab, Z. Nazli, H. N. Bhatti and S. Nouren, *J. Mol. Liq.*, 2018, **256**, 395–407.
- 42 A. D. Becke, *Phys. Rev. A: At., Mol., Opt. Phys.*, 1988, **38**, 3098–3100.
- 43 C. Lee, W. T. Yang and R. G. Parr, *Phys. Rev. B: Condens. Matter Mater. Phys.*, 1988, **37**, 785–789.
- 44 S. H. Vosko, L. Wilk and M. Nusair, *Can. J. Phys.*, 1980, **58**, 1200–1211.
- 45 A. D. Becke, *J. Chem. Phys.*, 1993, **98**, 5648–5652.
- 46 G. A. Petersson and M. A. Al-Laham, *J. Chem. Phys.*, 1991, **94**, 6081–6090.
- 47 A. D. McLean and G. S. Chandler, *J. Chem. Phys.*, 1980, **72**, 5639–5648.
- 48 R. Krishnan, J. S. Binkley, R. Seeger and J. A. Pople, *J. Chem. Phys.*, 1980, **72**, 650–654.